



An H α Imaging Survey of the Low-surface-brightness Galaxies Selected from the Fall Sky Region of the 40% ALFALFA HI Survey

Feng-Jie Lei^{1,2,3}, Hong Wu^{1,2,3}, Wei Du^{1,3}, Yi-Nan Zhu^{1,3}, Man-I Lam⁴, Zhi-Min Zhou^{1,3}, Min He^{1,2,3}, Jun-Jie Jin^{1,2,3}, Tian-Wen Cao^{1,2,3}, Pin-Song Zhao^{1,2,3}, Fan Yang^{1,3}, Chao-Jian Wu^{1,3}, Hong-Bin Li^{1,3}, and Juan-Juan Ren^{1,3}

¹ National Astronomical Observatories, Chinese Academy of Sciences, 20A Datun Road, Chaoyang District, Beijing, 100012, People's Republic of China; fjlei@nao.cas.cn, hwu@bao.ac.cn

² School of Astronomy and Space Science, University of Chinese Academy of Sciences, Beijing 100049, People's Republic of China

³ Key Laboratory of Optical Astronomy, National Astronomical Observatories, Chinese Academy of Sciences, Beijing 100012, People's Republic of China

⁴ Shanghai Astronomical Observatories, Chinese Academy of Sciences, 80 Nandan Road, Xuhui District, Shanghai, 200030, People's Republic of China

Received 2017 June 14; revised 2018 January 8; accepted 2018 January 12; published 2018 March 8

Abstract

We present the observed H α flux and derived star formation rates (SFRs) for a fall sample of low-surface-brightness galaxies (LSBGs). The sample is selected from the fall sky region of the 40% ALFALFA HI Survey–SDSS DR7 photometric data, and all the H α images were obtained using the 2.16 m telescope, operated by the National Astronomy Observatories, Chinese Academy of Sciences. A total of 111 LSBGs were observed and H α flux was measured in 92 of them. Though almost all the LSBGs in our sample are HI-rich, their SFRs, derived from the extinction and filter-transmission-corrected H α flux, are less than $1 M_{\odot} \text{ yr}^{-1}$. LSBGs and star-forming galaxies have similar HI surface densities, but LSBGs have much lower SFRs and SFR surface densities than star-forming galaxies. Our results show that LSBGs deviate from the Kennicutt–Schmidt law significantly, which indicates that they have low star formation efficiency. The SFRs of LSBGs are close to average SFRs in Hubble time and support previous arguments that most of the LSBGs are stable systems and they tend to seldom contain strong interactions or major mergers in their star formation histories.

Key words: galaxies: evolution – galaxies: star formation

1. Introduction

Low-surface-brightness galaxies (LSBGs) are galaxies whose central surface brightness is at least one magnitude fainter than the level of sky background in the dark night (Freeman 1970; Impey & Bothun 1997). Generally, they are defined as central surface brightness in the *B*-band $\mu_0(B) > 22.0\text{--}23.0 \text{ mag arcsec}^{-2}$ (Impey et al. 2001; Ceccarelli et al. 2012). LSBGs account for the bulk of the number of local galaxies, making them an important contributor to the baryon and dark matter mass budget in the local universe (O’Neil & Bothun 2000; Blanton et al. 2005; Boissier et al. 2016). Their morphologies and stellar populations distribute widely, ranging from old, high-metallicity early-type, to young, low-metallicity late-type galaxies (Bell et al. 2000). Even though the specific procedure of their formation and evolution is still unclear, their lower star formation rate (SFR) is consistent with the hypothesis that they are quiescent galaxies and have different star formation histories from their high surface brightness counterparts (McGaugh et al. 1995; Gerritsen & de Blok 1999; Boissier et al. 2008; Wyder et al. 2009; Schombert et al. 2013).

One of the most important parameters for understanding the evolution of galaxies is SFR. There are many approaches to deriving the SFR, utilizing the luminosity related to young massive stars, such as H α , UV, or IR luminosities, or fitting the observed spectral energy distribution with a model (Kennicutt 1998a; Silva et al. 1998; Wu et al. 2005; da Cunha et al. 2008; Zhu et al. 2008; Boselli et al. 2009; Noll et al. 2009; Wen et al. 2014; Jimmy et al. 2016). Among those SFR tracers,

H α emission is connected with photons whose wavelengths are shorter than 912 Å. These ionized photons are produced by young stars with ages of less than ~ 10 Myr and masses higher than $17 M_{\odot}$ (Watson et al. 2016). Therefore, compared to the approaches, the star formation timescale traced by H α emission is shorter.

Recent and ongoing H α image surveys provide a number of resources to study star formation. The H α 3 survey is an H α narrow band imaging survey of the Local and Coma Superclusters selected from ALFALFA (Haynes et al. 2011), which present the complete recent star formation and HI-rich galaxies in the Local Supercluster (Fossati et al. 2013; Gavazzi et al. 2013). Van Sistine et al. (2016) finished observations and data reduction for a fall sample of 656 galaxies from the HI Arcicibo Legacy Fast ALFA Survey (ALFALFA), the galaxies distances between ~ 20 and ~ 100 Mpc, but there was not a focus on LSBGs. There is an ongoing H α image survey of LSBGs selected from the PSS-II catalog (Schombert et al. 1992). However, only 59 LSBGs have been included in Schombert et al.’s (2011) sample. Consequently, up to now, there are only a few H α surveys of LSBGs, and the total number of LSBGs with available H α photometry is not large enough to derive confirming results. Therefore, we undertake an H α survey to follow up HI-selected LSBGs Galaxies from the 40% ALFALFA HI survey (Du et al. 2015), and we aim to study the SFR and star formation efficiency (SFE) of the HI-selected LSBGs.

There is an empirical relation between the gas surface density ($\Sigma_{\text{gas}} = \Sigma_{\text{H I} + \text{H}_2}$) and SFR surface density (Σ_{SFR}), ($\Sigma_{\text{SFR}} \propto \Sigma_{\text{gas}}^{1.4}$). Known as the Kennicutt–Schmidt Law, it reflects the relation between the large-scale SFR and the physical conditions in the interstellar medium (Schmidt 1959; Kennicutt 1998b; Bigiel et al. 2008, 2010; Boissier et al. 2008;

Leroy et al. 2008, 2013; Wyder et al. 2009; Boissier et al. 2016). However, such an empirical relation, generally derived on the basis of the samples of normal galaxies, might not be suitable for dwarf galaxies or LSBGs (Huang et al. 2012). Shi et al. (2011) proposed an “extended Schmidt Law,” which can be suitable for LSBGs.

In this paper, we present an $H\alpha$ survey for a sample of 111 LSBGs in the fall season in order to explore their SFRs and SFEs. This paper is organized as follows. In Section 2, we introduce our sample together with a description of the observations and data reduction. In Section 3, we present the catalog of $H\alpha$ flux and some derived parameters. Results and an analysis are given in Section 4, and a summary is provided in Section 5. Throughout the paper we adopt a flat Λ CDM cosmology, with $H_0 = 70 \text{ km s}^{-1} \text{ Mpc}^{-1}$ and $\Omega_\Lambda = 0.7$.

2. Sample Observations and Data Reduction

2.1. Sample

The ALFALFA Survey is a second-generation blind extragalactic HI survey and provides the first full census of HI-bearing objects over a cosmologically significant volume in the local Universe. This extragalactic HI survey is especially useful for studying low-mass, gas-rich objects in the local universe (Giovanelli et al. 2005; Haynes et al. 2011; Huang et al. 2014). This survey covers 7000 deg^2 and intends to detect more than 30,000 extragalactic HI sources. The first release covers 40% of the ALFALFA survey area and is called $\alpha.40$ (Haynes et al. 2011).

Du et al. (2015) constructed an LSBG sample with $\mu_0(B) > 22.5 \text{ mag arcsec}^{-2}$ from ALFALFA $\alpha.40$ in conjunction with SDSS DR7 photometry data (Abazajian et al. 2009), with an additional constraint on the axis ratio ($b/a > 0.3$) to prevent contamination from edge-on galaxies. Because the SDSS pipeline overestimates the level of sky background and underestimates the total magnitude of galaxies by about 0.2 mag, this value can reach 0.5 mag for LSBGs (Lisker et al. 2007; He et al. 2013). Du et al. (2015) reconstructed the sky background with a better method (Zheng et al. 1999; Wu et al. 2002; He et al. 2013) to get more accurate surface brightness. The galaxy geometric parameters (e.g., disk scale length in pixels, axis ratio) are fitted and obtained by the software GALFIT (Peng et al. 2002) and central surface brightness in the g -band and r -band are calculated by automagnitudes from the software SExtractor (Bertin & Arnouts 1996). The central surface brightnesses in the B -band are transformed from SDSS g - and r -band magnitudes. The final sample includes 1129 HI-rich LSBGs, which are defined as the main LSBG sample; hereafter they are referred to as Du2015.

Our sample contains fall objects (111) from Du2015 (1129) and is located within the region of $21^{\text{h}} < \text{R.A.} < 2^{\text{h}}$; $13^\circ < \text{decl.} < 16^\circ$ and $23^\circ < \text{decl.} < 33^\circ$. To obtain more accurate SFRs of LSBGs, an $H\alpha$ imaging survey is needed. We observed the $H\alpha$ images of a sample of 111 LSBGs located in the fall sky. All members of our LSBG sample belong to a blue cloud and are in a star formation sequence. We show the distributions of some photometric and HI parameters, including central surface brightness, heliocentric velocity, distance, radius containing 50% of Petrosian flux (r_{50}) in the SDSS r -band, HI mass, and stellar mass, of the LSBGs in our fall sample (royal blue) and Du2015 (sky blue) in Figure 1. All the HI parameters (heliovelocity, distance, HI mass) are derived

from the $\alpha.40$ catalog, and the heliocentric velocity of the HI source cz_\odot is in units of km s^{-1} (Haynes et al. 2011).

Central surface brightness and r_{50} and g , r magnitudes are from Du2015. The stellar mass is derived from the r -band magnitude and the $g - r$ color using the formula from Bell et al. (2003).

The distances used in this paper are estimated from two different approaches (Haynes et al. 2011). When the recession velocity (cz_\odot) of a galaxy is larger than 6000 km s^{-1} , the distance is estimated from cz_{cmb}/H_0 ; for those whose $cz_\odot < 6000 \text{ km s}^{-1}$, a velocity model is used (Haynes et al. 2011) to derive their distances. The peak of the HI mass distribution of our sample is $\log M_{\text{HI}}[M_\odot] \sim 9.7$. According to Huang et al. (2014) classification, 30% of LSBGs have high HI mass ($\log M_{\text{HI}}[M_\odot] \geq 9.5$), 65% of LSBGs have medium HI mass ($7.7 \leq \log M_{\text{HI}}[M_\odot] \leq 9.5$), and only 5% of LSBGs have low HI mass ($\log M_{\text{HI}}[M_\odot] \leq 7.7$). The peak of the stellar mass is around $10^{8.5} - 10^9 [M_\odot]$.

2.2. Observation

The observation for this LSBG sample ranged from 2014 to 2016, and the galaxies in our sample were taken in dark night. Both broad R -band and $H\alpha$ narrow band images were obtained with the BAO Faint Object Spectrograph and Camera (BFOSC) attached to the 2.16 m telescope at Xinglong observatory of the National Astronomical Observatories, Chinese Academy of Sciences (NAOC). The CCD frame of BFOSC is $1152 \times 1274 \text{ pixel}^2$, with a pixel scale of 0.45 arcsec , and has a field of view (FOV) of $8.5 \times 9.5 \text{ arcmin}^2$. The observation was made with a gain mode of $1.08 e^- \text{ ADU}^{-1}$ with a readout noise of $3 e^- \text{ pixel}^{-1}$. The FOV is suitable for acquiring images of galaxies with sizes of less than 3–4 arcmin, owing to the fact that accurate estimation of the sky background is essential for LSBGs.

Each observation adopts the same R -band filter and a suitable $H\alpha$ filter. The effective wavelength λ_{eff} of the broad R -band filter is 6407 \AA . There is a series of narrow band $H\alpha$ filters whose center wavelengths range from 6533 to 7052 \AA ($6533, 6589, 6631, 6701, 6749, 6804, 6851, 6900, 6948, 7000, \text{ and } 7052 \text{ \AA}$) with an FWHM of about 55 \AA . All the central wavelengths and FWHMs of the $H\alpha$ filters are shown in Table 1. The transmission curves of narrow $H\alpha$ filters are shown in Figure 2.

For each source, the R and $H\alpha$ images were taken with exposures of 300 s (R) and 1800 s ($H\alpha$ narrow band), respectively. The R -band integration time is deep enough to provide continuum subtraction for the narrow band image. The observation information is listed in Table 2.

2.3. Image Reduction

First, we check the quality of the images with the naked eye. After that, we reduce the CCD frames, including overscan subtraction, bias subtraction, flat-field correction, and cosmic-ray removal, following the standard image process with IRAF provided by NOAO.⁵ Then, the celestial coordinates are added to each image using *Astrometry.net*.

⁵ IRAF is the Image Analysis and Reduction Facility made available to the astronomical community by the National Optical Astronomy Observatories, which are operated by AURA, Inc., under contract with the US National Science Foundation. STSDAS is distributed by the Space Telescope Science Institute, which is operated by the Association of Universities for Research in Astronomy (AURA), Inc., under NASA contract NAS 526555.

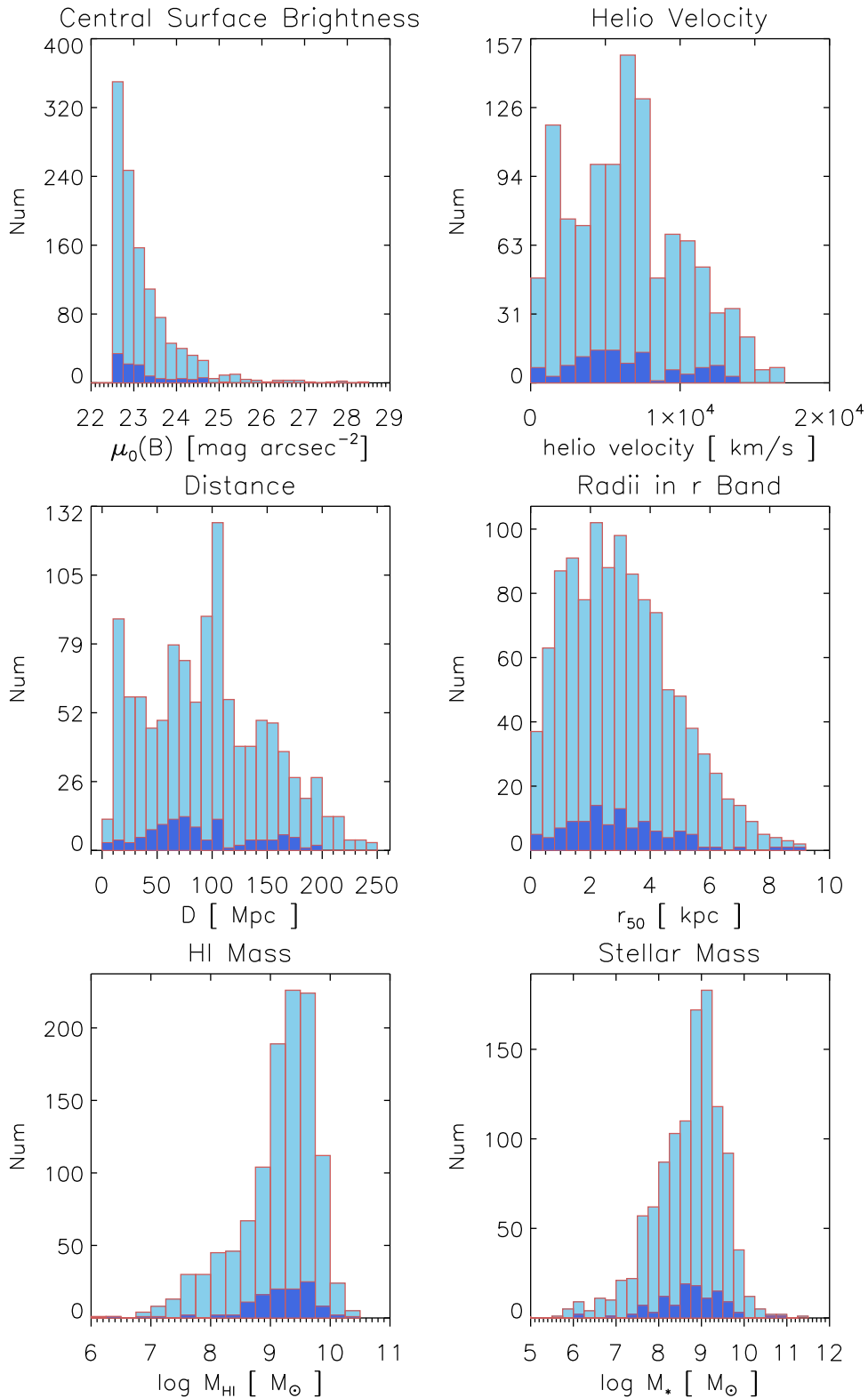


Figure 1. Photometric and HI parameters of our sample (royal blue) and the entire LSBG sample (sky blue) (Du et al. 2015). The parameters are B -band central surface brightness with a bin size of 0.25 mag (top left), heliocentric velocity with a bin size of 1000 km s^{-1} (top right), distance with a bin size of 10 Mpc (middle left), radius containing 50% of flux (r_{50}) in the SDSS r -band derived from Du et al. (2015; middle right), HI mass with a bin size of 0.25 (bottom left), and stellar mass derived from g - and r -band magnitudes with bin sizes of 0.25 (bottom right).

The next step is sky background construction, which is the most critical step of data reduction. SExtractor is employed to detect faint or extended objects in the Gaussian smoothed image. A mask image is produced after taking all the detected

objects off. In order to obtain the large-scale structures of the background, a median filter of $70 \times 70 \text{ pixel}^2$ is applied to the mask image to reduce the random noise and to fill in the mask regions with surrounding sky regions. The constructed sky

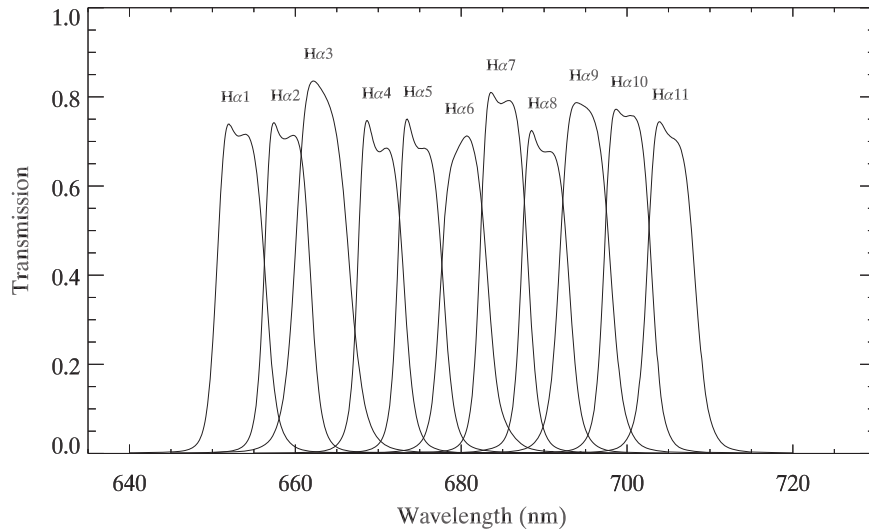


Figure 2. Transmission curve of H α filters from H α 1 to H α 11.

Table 1
The Properties of H α Narrow Band Filters

Filter	λ_c (Å)	FWHM (Å)
(1)	(2)	(3)
H α 1	6533	55
H α 2	6589	53
H α 3	6631	62
H α 4	6701	53
H α 5	6749	52
H α 6	6804	54
H α 7	6851	54
H α 8	6900	55
H α 9	6948	58
H α 10	7000	54
H α 11	7052	56

background image is subtracted from each image. Figure 3 shows an example of the original image, the constructed sky background, and the background-subtracted image; all three images are in the same value scale range. We can see that the sky background reflects the vignetting and non-uniformity distribution. We also compare the fluctuation of the original and sky-subtracted images in Figure 4. From Figure 4, the median distribution of the background after being sky-subtracted is closer to 0. The fluctuation of the sky-subtracted image (blue solid line) is much less than that of the original image (black dashed line).

Since the H α images contain contributions from both H α emission and the underlying stellar continuum, it is also important to remove the stellar continuum to get the real H α emission. Here, we adopt the *R*-band image as the stellar continuum, due to the fact that the wavelength coverage of the *R*-band is wide enough to be dominated by the stellar continuum. In order to subtract the continuum from the observed H α frames, we must scale the continuum flux of H α to same level as the flux of the *R*-band image. In this process, we assume that field stars have no H α emission, which means that they should have the same continuum flux ratios between H α and *R*-band images. Here, we define the count ratio of the

wide R_{band} and narrow H α band as WNCR:

$$\text{WNCR} = \frac{c_{W,\text{cont}}}{c_{N,\text{cont}}}. \quad (1)$$

Here, $c_{W,\text{cont}}$ and $c_{N,\text{cont}}$ are the measured count of the wide *R*-band and narrow H α band filters.

Statistically, the median WNCR of these field stars could be treated as the scale factor to subtract the continuum from the H α image. To obtain an accurate WNCR, we adopt aperture photometry, with radii 5 times the FWHM of the point-spread function for stars in each image, using SExtractor and selected field stars with S/N greater than 20. To match the continuum, H α image multiply WNCR and subtract the *R*-band image. It is tricky to adjust the value around WNCR to get the best scaled one. Finally the continuum is removed from scaled H α images, when the residual fluxes of most selected field stars reached a minimum.

The scaled values we used are from field stars, However, the scaled value of the object galaxies is somewhat different. The color of the studied galaxy is different from that of the field stars. The color effect of field stars would cause errors, leading to underestimates as large as 40% and overestimates as large as 10% when measuring H α equivalent width (Spector et al. 2012). To quantify the errors, we selected different spectral types (F, G, K) taken from the MILES stellar library. Because all our sample galaxies are located at high galactic latitude (82% sample $>30^\circ$) and M stars are too faint, only F G K stars were considered,;the WNCR error can be underestimated by as large as 7% and overestimated by as large as 7%.

Figure 5 shows the *R*-band, H α narrow band, and continuum-subtracted H α images of LSBG AGC 102243 from left to right, as an example. As Du2015 derived from the SDSS survey, the flux calibrations for the observed broad and narrow band images are undertaken depending on the SDSS photometry. The field stars with S/N > 20 in both SDSS and our *R*-band image are selected for flux calibration. Here, the aperture magnitudes of the SDSS *r*-band and *i*-band are used to calculate the Johnson *R*-band magnitudes based on Equation (2) (Lupton et al. 2005) as follows. The Johnson *R*-band magnitude is transformed to *AB* magnitude systems with Equation (3) (Frei & Gunn 1994). Then, the *AB* magnitude is transformed to flux density with

Table 2
The Observed Sample of LSBGs

AGC	$\mu_0(B)$ (magarcsec ⁻²)	R.A. J2000	Decl. J2000	z	Dist (Mpc)	Filter	Date
(1)	(2)	(3)	(4)	(5)	(6)	(7)	(8)
17	23.4405	00:03:43	+15:13:05	0.0029	12.8	Ha1	20140102
273	22.6556	00:28:07	+25:59:47	0.0187	78.9	Ha4	20140819
337	22.5591	00:34:25	+24:36:13	0.0178	74.9	Ha3	20141021
1084	23.6324	01:31:22	+23:57:14	0.0114	46.4	Ha3	20160206
1211	23.1475	01:43:55	+13:48:22	0.0080	32.4	Ha2	20141017
1362	22.9079	01:53:51	+14:45:50	0.0264	109.1	Ha5	20160108
1693	23.2348	02:12:03	+14:06:14	0.0127	52.1	Ha3	20131010
2144	22.7754	02:39:30	+29:15:35	0.0160	65.5	Ha3	20141021
12289	22.6539	22:59:41	+24:04:29	0.0339	140.2	Ha6	20140826
12845	22.7974	23:55:42	+31:53:59	0.0162	69.1	Ha3	20141021
100037	22.9236	00:06:03	+27:20:54	0.0106	44.8	Ha2	20160205
100350	23.9767	00:37:44	+24:12:28	0.0155	65.0	Ha3	20131231
101191	23.2293	00:23:39	+15:04:03	0.0177	74.7	Ha3	20131010
101812	23.6638	00:08:49	+14:02:01	0.0064	27.0	Ha2	20131230
101877	23.0745	00:02:15	+14:29:16	0.0172	72.9	Ha3	20131010
101942	22.9001	00:12:29	+15:33:22	0.0188	79.7	Ha4	20131010
101986	22.8072	00:20:49	+15:03:13	0.0254	104.0	Ha4	20140825
102098	22.6041	00:39:04	+14:36:01	0.0418	174.1	Ha7	20160208
102101	23.0727	00:39:25	+14:27:23	0.0180	75.6	Ha3	20140819
102229	22.5805	00:38:24	+25:26:10	0.0110	45.9	Ha2	20141017
102243	22.5023	00:05:05	+23:58:11	0.0219	89.0	Ha4	20140825
102302	22.9648	00:12:48	+14:31:31	0.0061	25.7	Ha2	20131230
102558	23.0152	00:07:05	+27:01:28	0.0099	41.7	Ha2	20160205
102630	24.6769	00:13:13	+25:36:14	0.0208	88.4	Ha4	20140101
102635	22.5726	00:16:12	+24:50:57	0.0316	130.8	Ha5	20151210
102672	22.5757	00:46:24	+25:04:14	0.0176	73.9	Ha3	20140819
102674	23.3246	00:49:14	+25:17:35	0.0463	193.8	Ha7	20141017
102684	23.9342	00:22:07	+25:29:09	0.0248	101.6	Ha4	20141018
102728	22.8543	00:00:21	+31:01:19	0.0019	9.1	Ha1	20140101
102729	22.5906	00:00:32	+30:52:09	0.0154	65.4	Ha3	20131231
102730	22.6859	00:00:39	+31:56:18	0.0421	175.8	Ha7	20141017
102900	25.0466	00:04:39	+29:35:56	0.0405	168.6	Ha6	20140827
102981	22.5401	00:02:56	+28:16:38	0.0153	64.8	Ha3	20140820
110150	22.7571	01:14:45	+27:08:06	0.0121	49.5	Ha3	20140819
110319	24.6744	01:25:17	+14:08:55	0.0168	69.9	Ha3	20141021
110379	23.5195	01:30:15	+14:40:39	0.0082	33.1	Ha2	20141017
110398	22.5212	01:31:46	+14:09:20	0.0225	92.3	Ha4	20140825
112503	22.5698	01:38:00	+14:58:58	0.0025	10.2	Ha1	20141017
112892	22.5765	01:20:16	+14:52:29	0.0370	154.3	Ha6	20160210
113200	22.7375	01:56:19	+14:55:29	0.0248	102.3	Ha4	20160210
113752	23.1777	01:18:06	+27:11:17	0.0414	173.3	Ha6	20140827
113790	23.2295	01:13:02	+27:38:13	0.0165	68.7	Ha3	20140826
113825	22.8080	01:43:27	+24:46:47	0.0128	52.4	Ha3	20141021
113845	22.7484	01:17:22	+24:08:16	0.0273	112.7	Ha5	20160108
113907	22.6913	01:13:56	+30:09:25	0.0342	142.5	Ha6	20160208
113918	22.8345	01:22:59	+32:10:44	0.0355	148.1	Ha6	20160208
113923	23.2240	01:26:13	+32:08:11	0.0140	57.6	Ha3	20140819
114040	22.6830	01:18:27	+29:06:55	0.0262	108.0	Ha4	20141018
121174	26.3089	02:38:16	+29:54:23	0.0023	9.7	Ha1	20141017
122138	27.1803	02:33:16	+28:10:44	0.0034	13.7	Ha1	20131230
122210	23.3301	02:31:33	+26:47:49	0.0152	62.2	Ha3	20140826
122211	23.9519	02:31:37	+26:32:32	0.0123	49.8	Ha3	20141021
122341	22.8250	02:11:29	+14:28:04	0.0375	156.8	Ha6	20160208
122874	22.6132	02:26:15	+24:26:02	0.0213	87.8	Ha4	20151210
122877	24.1814	02:27:32	+24:52:12	0.0203	85.0	Ha4	20160210
122884	23.1394	02:32:53	+25:09:11	0.0081	32.4	Ha2	20141017
122924	24.0678	02:34:43	+24:29:12	0.0322	134.5	Ha5	20160207
123046	23.0294	02:41:12	+31:29:29	0.0160	65.7	Ha3	20141021
123047	23.0369	02:41:48	+31:27:26	0.0340	142.7	Ha6	20141017
123170	22.8858	02:44:03	+29:17:17	0.0030	12.1	Ha1	20141017
123172	22.5982	02:47:23	+29:10:32	0.0180	74.5	Ha3	20151204
320466	24.4058	22:57:22	+27:58:50	0.0098	43.3	Ha2	20131230

Table 2
(Continued)

AGC	$\mu_0(B)$ (magarcsec ⁻²)	R.A. J2000	Decl. J2000	z	Dist (Mpc)	Filter	Date
(1)	(2)	(3)	(4)	(5)	(6)	(7)	(8)
321166	24.0888	22:55:49	+14:45:15	0.0094	41.3	Ha2	20131230
321341	22.7167	22:52:16	+24:06:09	0.0404	168.3	Ha6	20140827
321348	23.0037	22:47:44	+23:59:59	0.0315	129.9	Ha5	20140826
321385	22.5978	22:59:15	+24:42:34	0.0242	98.5	Ha4	20141018
321429	23.6289	22:41:27	+31:31:48	0.0126	55.6	Ha3	20131231
321435	22.6576	22:47:44	+32:11:18	0.0129	56.6	Ha3	20140819
321438	24.0373	22:50:17	+30:15:08	0.0265	108.6	Ha5	20140101
321451	22.5598	22:48:03	+29:49:48	0.0237	96.8	Ha4	20140820
321490	23.2068	22:47:45	+28:54:26	0.0233	95.0	Ha4	20140825
321492	23.1417	22:53:23	+29:00:52	0.0068	30.8	Ha2	20131230
331052	22.9473	23:59:45	+27:15:14	0.0156	66.5	Ha3	20140819
332431	22.8894	23:07:46	+14:22:34	0.0246	100.3	Ha4	20140820
332640	23.0183	23:24:43	+13:48:36	0.0265	108.2	Ha5	20140825
332761	23.0965	23:31:11	+15:01:58	0.0193	82.6	Ha4	20140825
332786	22.5704	23:36:09	+15:44:38	0.0134	57.5	Ha3	20131229
332844	22.8276	23:51:24	+14:14:02	0.0394	163.5	Ha6	20141021
332861	22.5843	23:53:04	+14:35:07	0.0263	107.5	Ha5	20140825
332879	22.7499	23:56:44	+15:27:36	0.0265	108.5	Ha5	20131010
332887	23.4223	23:58:44	+16:05:26	0.0196	83.2	Ha4	20141018
332906	23.3617	23:05:09	+25:52:28	0.0327	135.1	Ha5	20140101
333224	22.9186	23:59:24	+26:32:53	0.0257	105.4	Ha4	20140101
333318	22.7712	23:10:39	+24:08:40	0.0410	170.5	Ha6	20140827
333442	22.6876	23:58:33	+31:07:47	0.0320	132.5	Ha5	20160108
748648	23.4768	21:44:47	+15:24:26	0.0378	157.3	Ha6	20140827
748715	22.7025	22:39:38	+13:57:58	0.0208	89.8	Ha4	20140825
748723	23.7324	22:52:04	+15:12:20	0.0373	154.7	Ha6	20140827
748724	22.8417	22:55:07	+14:48:04	0.0314	129.6	Ha5	20131228
748737	22.9517	23:03:03	+14:10:13	0.0247	100.6	Ha4	20141018
748738	24.3426	23:04:52	+14:01:05	0.0130	56.5	Ha3	20131231
748744	23.1245	23:09:16	+14:21:58	0.0163	70.5	Ha3	20140819
748757	22.5773	23:19:04	+16:01:20	0.0130	56.1	Ha3	20140819
748763	22.7211	23:23:32	+13:50:16	0.0437	182.2	Ha7	20141017
748765	24.5539	23:23:43	+14:25:40	0.0116	50.0	Ha3	20140826
748766	23.3312	23:23:48	+14:56:50	0.0425	177.0	Ha7	20140102
748767	23.3730	23:24:11	+15:53:10	0.0144	61.8	Ha3	20140826
748769	24.4649	23:26:14	+15:04:41	0.0140	60.1	Ha3	20140826
748770	23.0814	23:27:29	+14:48:48	0.0407	169.4	Ha6	20140827
748777	24.2502	00:03:11	+15:02:40	0.0460	192.1	Ha7	20141017
748778	24.5455	00:06:34	+15:30:39	9.0E-4	4.6	Ha1	20140102
748786	23.7866	00:23:06	+15:08:21	0.0184	77.7	Ha3	20140819
748788	22.8876	00:24:10	+15:59:38	0.0174	73.5	Ha3	20141021
748790	23.1116	00:25:07	+14:22:06	0.0180	75.9	Ha3	20131229
748794	24.1651	00:39:28	+14:37:07	0.0177	74.3	Ha3	20131228
748795	22.5902	00:40:56	+14:14:08	0.0387	161.1	Ha6	20160209
748798	24.6805	00:49:01	+14:03:05	0.0386	160.6	Ha6	20160209
748805	22.8382	01:04:36	+15:16:21	0.0144	59.6	Ha3	20141021
748815	22.6130	01:27:03	+14:39:38	0.0216	88.0	Ha4	20140825
748817	22.5455	01:28:33	+15:14:54	0.0211	86.2	Ha4	20141018
748819	24.6432	01:37:25	+14:39:37	0.0086	35.0	Ha2	20160207

Equation (4).

$$R = r - 0.2936(r - i) - 1.439; \sigma = 0.0072, \quad (2)$$

$$R(AB) = R + 0.055, \quad (3)$$

$$m_{AB} = -2.5 \log_{10} \left(\frac{f_{\nu}}{3631 JY} \right). \quad (4)$$

Based on this formula, we derive the averaged calibration factor (flux density per count) of each image, which is then

applied to calibrating the photometric fluxes in both R -band and continuum-subtracted $H\alpha$ images.

2.4. Photometry

An elliptical aperture is adopted to perform photometry on both R -band and $H\alpha$ band images. First, the broad R -band image is used to determine photometric radius. Helped by the IRAF task ellipse, we can obtain the profile of the total flux counts enclosed by an elliptical aperture, along with the semimajor axis. Then, the



Figure 3. Example of the sky background subtraction of LSBG AGC 102672. All images are $9'0 \times 8'3$, and the length of the yellow line is $2'$. The left panel is the original R -band image. The middle panel is the constructed R -band sky background, and the right panel is the sky-background-subtracted image. All three images are in the same scale range.

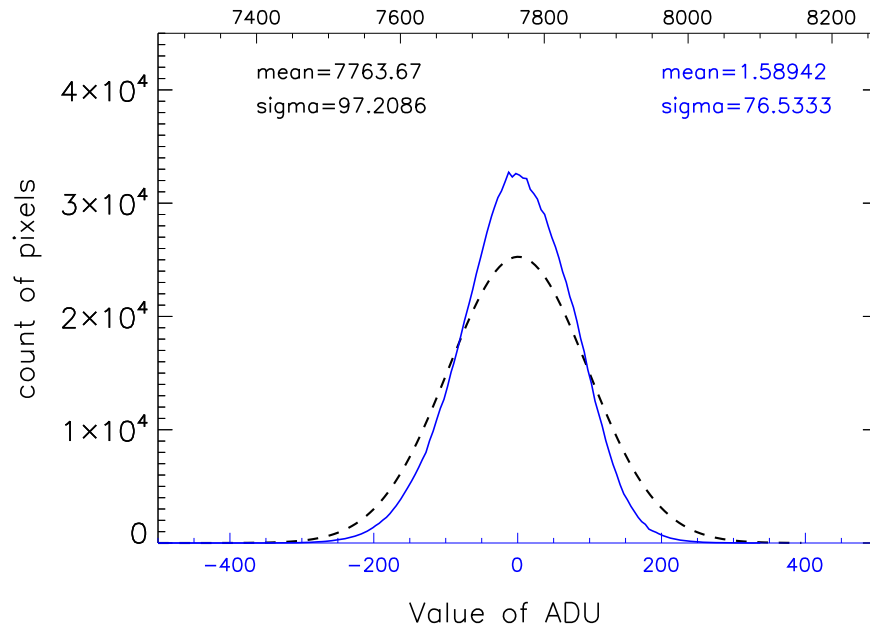


Figure 4. Example of distributions of the global background fluctuations of LSBG AGC 102672 before (black dashed line) and after (blue solid line) background subtraction. A Gaussian fitting is applied to the two distributions. The upper portion of the panel gives the mean values and standard deviations of the two distributions.

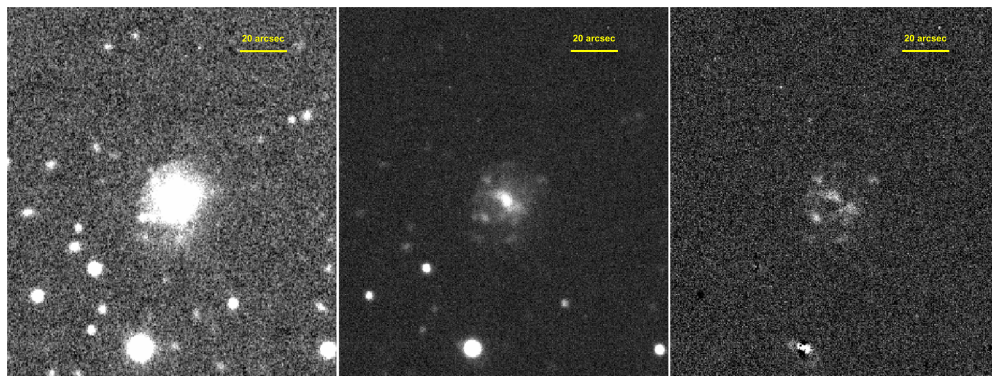


Figure 5. Example images of LSBG AGC 102243 showing the process of continuum subtraction. R -band, $H\alpha$ band, and continuum-subtracted $H\alpha$ images are shown in this figure from left to right.

flux at which the growth curve reaches $25 \text{ mag arcsec}^{-2}$, the semimajor axis (a), and the semi-minor axis (b) are adopted as the optical photometry radius. $H\alpha$ flux is total flux enclosed by elliptical area. There are 111 objects in total and 19 objects cannot be detected because of their weak $H\alpha$ emission.

3. $H\alpha$ Flux of LSBGs

3.1. Flux Correction

Taking the $H\alpha$ filter transmission curve into account, we adopt the transmission curve of $H\alpha$ filters in Figure 2 and

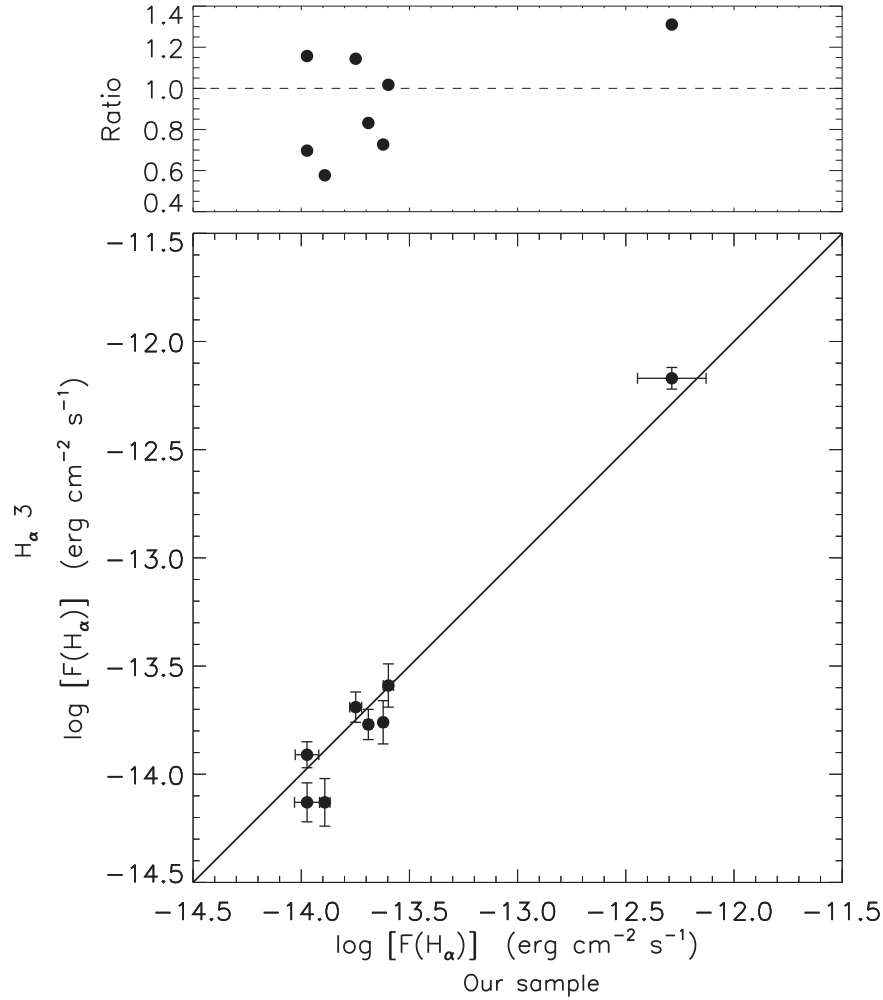


Figure 6. Comparison of the H α flux of eight LSBGs between our measurements and the H α 3 survey. The upper panel is the ratio value ($\text{Flux}_{\text{H}\alpha 3}/\text{Flux}_{\text{our sample}}$) between H α 3 flux and our sample.

correct the transmission loss brought by the H α filters. The normalized transmission $T(\text{H}\alpha)$ used for correcting the flux is derived from the equation

$$T(\text{H}\alpha) = \frac{T'(\text{H}\alpha)}{\int_{\lambda_1}^{\lambda_2} T'(\lambda) d\lambda / \text{FWHM}}, \quad (5)$$

where $T'(\lambda)$ is the transmission curve, $T'(\text{H}\alpha)$ is the direct transmission at the galaxy-redshifted H α wavelength from the transmission curve, $T(\text{H}\alpha)$ is the normalized transmission at the galaxy-redshifted H α wavelength, and λ_1 and λ_2 are the starting and ending wavelengths of the transmission curve. FWHM is the full width at half maximum of the H α filters. The corrected H α flux is obtained after dividing the normalized transmission $T(\text{H}\alpha)$.

The bandwidth of the R -band filter we used is wide enough, which leads to the fact that, apart from the stellar continuum, the observed flux in the R filter still contains the contribution from H α emission, which will result in the loss of H α flux during the process of stellar continuum subtraction. Fortunately, such a loss can be estimated (about 4%) and corrected according to the bandwidth of both the R and H α filters.

The extinctions for the galaxies in our sample include the contributions from both Galactic and intrinsic extinctions. For nearby galaxies, their H α emission feature is covered by the SDSS

r filter. Therefore, we adopt the extinction value in the SDSS r -band to correct observed H α Galactic extinction. Generally, intrinsic extinction correction is derived from the Balmer emission line ratio of $F_{\text{H}\alpha}/F_{\text{H}\beta}$. The color excess $E(B - V)$ can be derived from $[F_{\text{H}\alpha}/F_{\text{H}\beta}]/[F_{\text{H}\alpha 0}/F_{\text{H}\beta 0}]$, according to CCM extinction law (Cardelli et al. 1989). Here, we adopt the intrinsic ratio $F_{\text{H}\alpha 0}/F_{\text{H}\beta 0}$ as 2.87 for H II galaxies, then the extinction correction of H α flux is calculated from $A_{\text{H}\alpha} = 2.468 E(B - V)$ (Calzetti 2001). However, only 20% of the LSBGs in our fall sample have nuclear fiber spectra from SDSS. Therefore, we have to adopt the same extinction correction and assume that there is no extinction gradient for all sample LSBGs. In total, 510 LSBGs from Du2015 have available SDSS spectra and Balmer ratios $F_{\text{H}\alpha}/F_{\text{H}\beta}$ derived from the MPA-JHU catalog of SDSS DR7. Finally, we adopt a median value of $F_{\text{H}\alpha}/F_{\text{H}\beta} = 3.1493$ for the 510 LSBGs as the extinction correction for all sample LSBGs.

Owing to the approximate 60 Å FWHM bandwidth of those H α filters, [N II] $\lambda\lambda 6548, 6584$ features also contribute to the obtained H α images. We can remove these [N II] features following Equation (6), with the assumption of a fixed ratio of [N II]/H α throughout all the galaxies:

$$f_{\text{H}\alpha, \text{corr}[\text{N II}]} = \frac{f_{\text{H}\alpha + \text{N}[\text{II}]}}{1 + \frac{f_{\text{N}[\text{II}]}}{f_{\text{H}\alpha}}}. \quad (6)$$

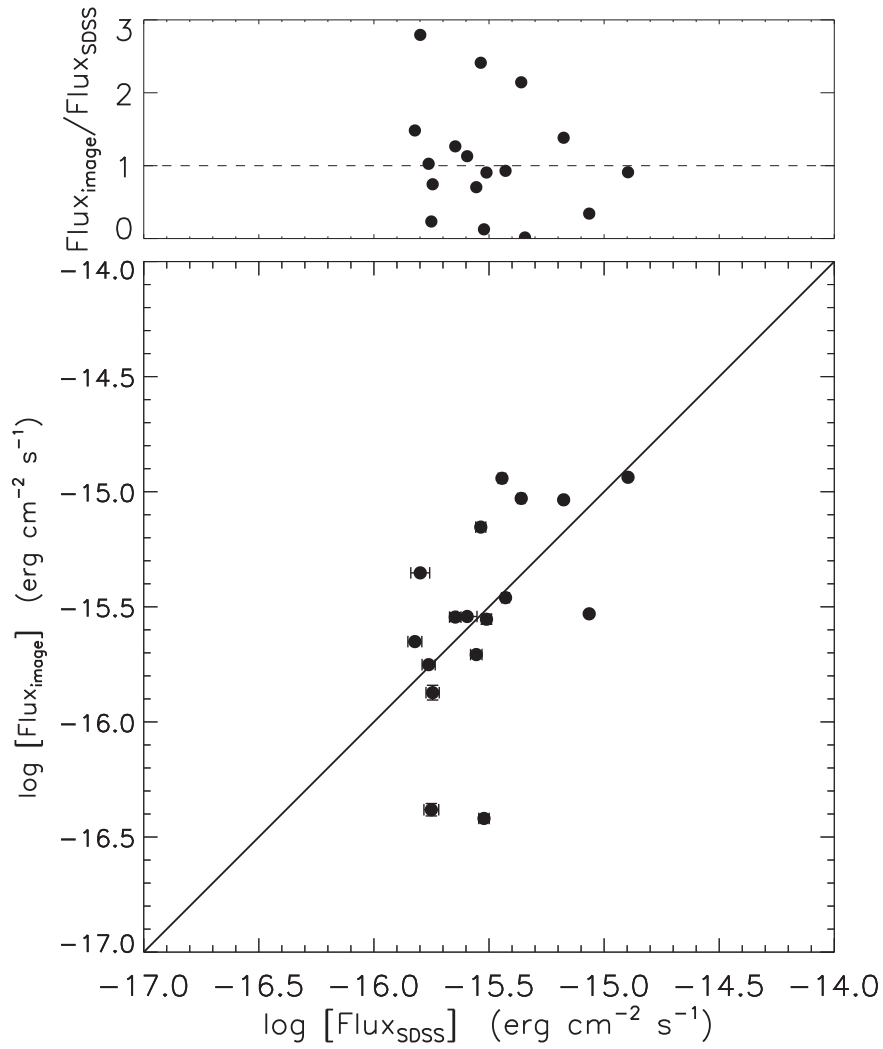


Figure 7. Comparison of our sample flux from our $H\alpha$ image and the SDSS fiber spectra flux within $3''$. The upper panel shows the flux ratio between the $H\alpha$ image and SDSS spectra.

Similar to intrinsic extinction correction, we take the median ratio 0.1578 of $[N II]/H\alpha$ for all 510 LSBGs with available SDSS fiber spectra, and apply it to $[N II]$ correction for all the galaxies in our sample.

3.2. $H\alpha$ Flux and Reliability

After all the corrections above, we get the total $H\alpha$ flux for each LSBG. In order to compare with previous works, we check eight LSBGs from our spring sample that also belong to the $H\alpha 3$ survey (Gavazzi et al. 2015). Figure 6 shows a comparison between the LSBG fluxes estimated by us and those derived from the $H\alpha 3$ survey, and the upper panel shows the ratio between the $H\alpha 3$ survey flux and ours. The differences between them are around 0.1 dex and less than 0.18 dex. Roughly speaking, these two calibrated $H\alpha$ fluxes are consistent.

Since 20% of the LSBGs in our fall sample have SDSS fiber spectra, the $H\alpha$ flux can also be derived directly from the MPA-JHU directly. We first measure the $H\alpha$ flux on the image within the SDSS fiber diameter ($3''$) and then compare with $H\alpha$ flux from SDSS fiber spectra in Figure 7. Most of the $H\alpha$ flux is consistent. There are two objects that deviate far away from the SDSS fiber flux. After checking with an $H\alpha$ image we

found that there is no detectable $H\alpha$ emission where the fiber is located.

We also check the SFR of these LSBGs. Due to the $3''$ fiber diameter, an aperture correction is needed to get the total $H\alpha$ flux of the whole galaxy. Here, we assume that the $H\alpha$ emission follows the same distribution as the SDSS r -band image. The value of the aperture correction can be calculated from the difference between the fiber and Petrosian magnitudes in the r -band as follows:

$$F_{\text{Petro}}/F_{\text{Fiber}} = 10^{-0.4(m_{\text{petro}} - m_{\text{fiber}})}. \quad (7)$$

Here, m_{petro} and m_{fiber} are the Petrosian and fiber magnitudes in the r -band, respectively. F_{Fiber} represents the $H\alpha$ flux of a galaxy in the given fiber aperture, whereas F_{petro} is the total $H\alpha$ flux inside the Petrosian aperture.

$H\alpha$ emission traces the location of the star formation region and also provides a fairly robust quantitative measure of its current SFR. The SFR of the LSBGs in our sample is calculated from the $H\alpha$ luminosity using the following calibration (Kennicutt 1998b):

$$\text{SFR}_{H\alpha}(M_{\odot} \text{ yr}^{-1}) = 7.9 \times 10^{-42} [L(H\alpha)](\text{erg s}^{-1}), \quad (8)$$

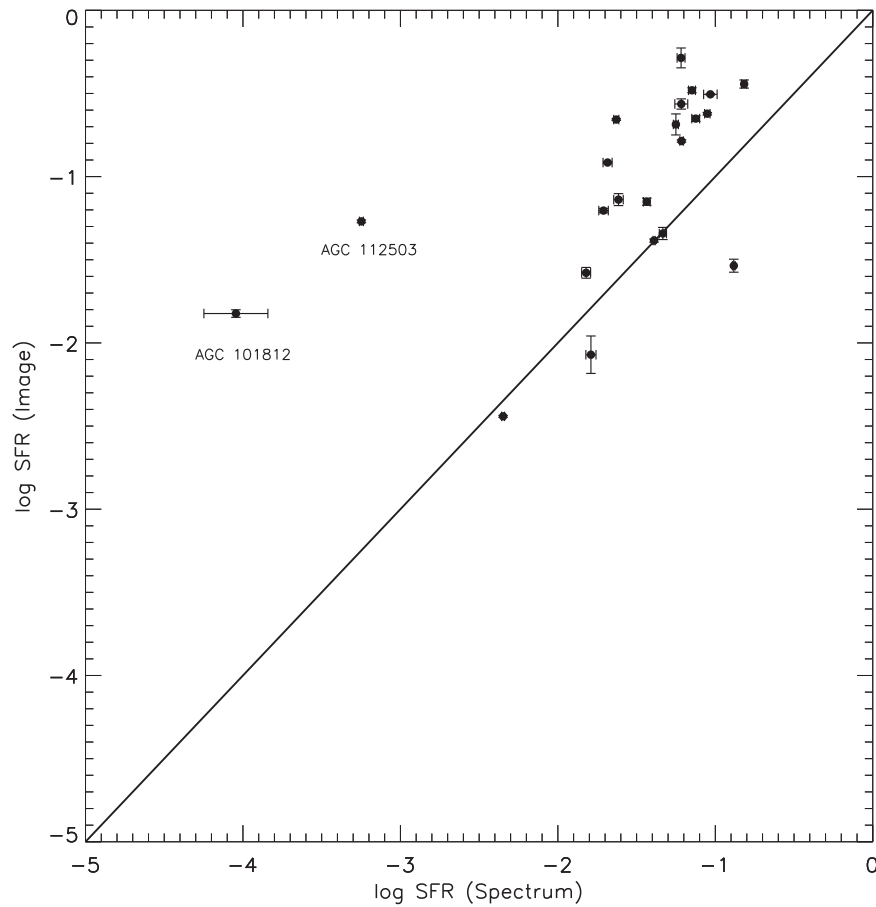


Figure 8. Comparison of the measured SFRs of 22 LSBGs derived by our $H\alpha$ images and by aperture-corrected SDSS fiber spectra.

where $L(H\alpha)$ is the intrinsic extinction-corrected $H\alpha$ luminosity. The initial mass function used in the conversion is a Salpeter function [$dN(m)/dm = -2.35$] over $m = 0.1-100 M_{\odot}$. Figure 8 shows a comparison between the SFRs of LSBGs calculated from an $H\alpha$ image and $H\alpha$ spectrum. For most of the LSBGs in our sample, the SFRs derived from SDSS spectra are less than those from $H\alpha$ images, and there are two LSBGs (AGC 101812, AGC 112503) showing large deviations, probably due to the aperture correction. Checking with the SDSS images of AGC 101812 and AGC 112503 shows that there exist several bright blue knots outside of the fiber region. Thus, aperture corrections have largely underestimated the total $H\alpha$ emission. Therefore, it is inadequate to calculate the total $H\alpha$ flux for the entire galaxy solely from the fiber spectrum.

All the $H\alpha$ flux and other basic parameters of LSBGs are listed in Table 3. The table columns can be briefly described as follows:

- Column 1: galaxy name in terms of AGC number.
- Column 2: the semimajor axis from elliptical photometry (kpc), which is the radii at 25 magarcsec⁻².
- Column 3: the ellipticity from the elliptical photometry.
- Columns 4 and 5: logarithm of the $H\alpha$ flux and error ($\text{erg s}^{-1} \text{cm}^{-2}$).
- Column 6: the logarithm of the SFR ($M_{\odot} \text{yr}^{-1}$).
- Column 7: the logarithm of the SFR surface density ($M_{\odot} \text{yr}^{-1} \text{kpc}^{-2}$).

Column 8: the logarithm of the H I mass taken from the $\alpha.40$ catalog (Haynes et al. 2011).

Column 9: the logarithm of the H I gas surface density ($M_{\odot} \text{pc}^{-2}$).

We will explore the SFR and SFR surface density, and H I gas and H I gas surface density in the next section.

4. Results and Analysis

4.1. The Star Formation and Gas Surface Density

For each LSBG in our sample, the enclosed region of elliptical photometry is used as the optical area to calculate the star formation surface density (Σ_{SFR}). For the majority of the targets, the beam size of ALFALFA H I observation is 3.5 arcmin, which is too large to obtain a suitable H I size. Hence, we have to derive the H I size from the calibrated optical photometry size. $r_{\text{H I}}/r_{25}$ is almost constant (1.7 ± 0.5) and shows weak dependence on the type from S0 to Im (Broeils & Rhee 1997; Swaters & Balcells 2002; Jaskot et al. 2015). We adopt 1.7 times the optical photometry radii as the H I radii. Hence, the H I surface density $\Sigma_{\text{H I}}$ is calculated from the following equation:

$$\Sigma_{\text{H I}} = \frac{M_{\text{H I}}}{\pi (1.7^2 ab)}. \quad (9)$$

Here, $M_{\text{H I}}$ is the H I mass derived from the ALFALFA catalog, and a and b are the semimajor and semi-minor radii of photometry ellipticals, respectively. SFE is defined as the ratio

Table 3
The Star Formation Properties of LSBGs

AGC	r_{25} (Kpc)	Ellipse	$\log F(\text{H}\alpha)$ ($\text{erg cm}^{-2} \text{s}^{-1}$)	$\log \sigma(F(\text{H}\alpha))$ ($\text{erg cm}^{-2} \text{s}^{-1}$)	$\log(\text{SFR})$ ($M_{\odot} \text{yr}^{-1}$)	$\log \Sigma_{\text{sfr}}$ ($M_{\odot} \text{yr}^{-1} \text{Kpc}^{-2}$)	$\log M_{\text{H I}}$ (M_{\odot})	$\log \Sigma_{\text{H I}}$ ($M_{\odot} \text{pc}^{-2}$)
(1)	(2)	(3)	(4)	(5)	(6)	(7)	(8)	(9)
17	2.63	0.24	8.41	0.73
273	9.40	0.32	-14.64	0.08	-1.87	-4.15	9.59	0.85
337	8.47	0.26	-12.93	0.01	-0.20	-2.43	9.88	1.20
1084	5.67	0.47	-13.78	0.02	-1.47	-3.19	9.50	1.31
1211	6.89	0.33	-13.30	0.01	-1.30	-3.30	8.98	0.52
1362	12.44	0.23	-13.73	0.01	-0.68	-3.25	9.36	0.33
1693	9.27	0.07	-13.22	0.01	-0.81	-3.21	9.49	0.63
2144	9.66	0.20	-12.96	0.01	-0.35	-2.72	9.18	0.35
12289	24.96	0.11	-13.17	0.01	0.10	-3.14	10.30	0.60
12845	25.03	0.20	-11.67	0.01	0.98	-2.22	10.18	0.52
100037	6.07	0.20	-13.35	0.01	-1.07	-3.04	8.76	0.33
100350	5.27	0.20	-14.23	0.04	-1.63	-3.47	8.92	0.62
101191	5.83	0.33	-13.44	0.01	-0.72	-2.57	8.95	0.63
101812	1.89	0.20	-13.94	0.02	-2.11	-3.06	8.73	1.31
101877	7.87	0.50	-13.97	0.01	-1.27	-3.26	9.57	1.12
101942	5.68	0.45	-14.96	0.10	-2.18	-3.93	9.14	0.93
101986	8.54	0.20	-13.70	0.01	-0.69	-2.95	9.33	0.61
102098	9.30	0.34	9.68	0.97
102101	8.39	0.35	-13.78	0.02	-1.04	-3.20	9.21	0.59
102229	9.68	0.20	8.94	0.11
102243	8.99	0.24	-13.52	0.01	-0.65	-2.93	9.78	1.03
102302	2.04	0.20	-15.01	0.18	-3.22	-4.24	8.79	1.31
102558	8.66	0.03	8.27	-0.55
102630	5.89	0.20	-14.11	0.05	-1.24	-3.18	9.17	0.77
102635	12.82	0.14	-13.56	0.01	-0.35	-3.00	9.65	0.54
102672	4.19	0.29	-13.16	0.01	-0.44	-2.04	9.20	1.15
102674	13.94	0.12	-13.97	0.01	-0.42	-3.15	10.02	0.83
102684	8.57	0.43	-13.80	0.04	-0.81	-2.93	9.27	0.69
102728	0.23	0.20	-14.47	0.06	-3.58	-2.70	6.78	1.20
102729	4.81	0.34	-13.59	0.01	-0.99	-2.67	8.85	0.71
102730	10.12	0.22	-14.00	0.01	-0.54	-2.94	9.68	0.82
102900	16.24	0.20	-14.02	0.03	-0.59	-3.41	9.81	0.53
102981	7.72	0.20	8.72	0.08
110150	6.78	0.05	-13.33	0.01	-0.97	-3.10	9.49	0.89
110319	5.55	0.20	-14.13	0.02	-1.46	-3.35	9.22	0.87
110379	2.72	0.16	-13.88	0.01	-1.86	-3.15	9.20	1.45
110398	12.53	0.42	-13.40	0.01	-0.50	-2.95	9.63	0.71
112503	1.22	0.55	-13.42	0.01	-2.43	-2.75	7.14	0.36
112892	10.28	0.20	-13.79	0.05	-0.44	-2.86	9.54	0.66
113200	5.18	0.20	-13.91	0.06	-0.92	-2.75	9.29	1.00
113752	17.34	0.20	9.72	0.38
113790	5.30	0.20	8.57	0.26
113825	2.13	0.20	-14.66	0.05	-2.24	-3.30	8.98	1.46
113845	4.70	0.28	-14.43	0.02	-1.35	-3.05	9.25	1.09
113907	8.61	0.10	-13.96	0.02	-0.67	-3.00	9.36	0.58
113918	9.87	0.11	9.47	0.57
113923	3.34	0.20	-14.12	0.01	-1.63	-3.08	9.05	1.14
114040	8.07	0.42	-14.83	0.34	-1.79	-3.86	9.40	0.86
121174	0.88	0.20	8.18	1.43
122138	1.25	0.20	-14.25	0.04	-3.00	-3.59	8.08	1.02
122210	6.27	0.23	-13.46	0.01	-0.90	-2.88	9.29	0.85
122211	3.97	0.32	-13.96	0.02	-1.59	-3.11	8.66	0.67
122341	14.42	0.45	-13.95	0.03	-0.59	-3.14	9.90	0.88
122874	5.05	0.37	-14.29	0.02	-1.43	-3.13	9.12	0.96
122877	8.55	0.80	9.18	1.06
122884	2.93	0.33	-14.03	0.02	-2.03	-3.29	9.17	1.45
122924	4.05	0.19	9.50	1.42
123046	8.51	0.07	-13.30	0.03	-0.69	-3.01	8.89	0.10
123047	6.42	0.45	-13.98	0.02	-0.69	-2.55	9.47	1.16
123170	1.29	0.20	7.68	0.60
123172	5.77	0.30	-13.96	0.02	-1.24	-3.10	9.25	0.92
320466	5.71	0.35	9.13	0.85

Table 3
(Continued)

AGC	r_{25} (Kpc)	Ellipse	$\log F(\text{H}\alpha)$ ($\text{erg cm}^{-2} \text{s}^{-1}$)	$\log \sigma(F(\text{H}\alpha))$ ($\text{erg cm}^{-2} \text{s}^{-1}$)	$\log(\text{SFR})$ ($M_{\odot} \text{ yr}^{-1}$)	$\log \Sigma_{\text{sfr}}$ ($M_{\odot} \text{ yr}^{-1} \text{ Kpc}^{-2}$)	$\log M_{\text{H I}}$ (M_{\odot})	$\log \Sigma_{\text{H I}}$ ($M_{\odot} \text{ pc}^{-2}$)
(1)	(2)	(3)	(4)	(5)	(6)	(7)	(8)	(9)
321166	6.48	0.20	8.62	0.14
321341	11.90	0.26	-14.13	0.03	-0.70	-3.22	9.66	0.68
321348	9.64	0.31	-13.73	0.01	-0.53	-2.84	9.52	0.75
321385	3.95	0.35	-14.19	0.02	-1.23	-2.73	9.32	1.36
321429	1.74	0.56	-15.53	0.20	-3.06	-3.69	8.55	1.47
321435	4.74	0.61	-13.29	0.01	-0.81	-2.25	8.88	0.98
321438	4.32	0.39	-15.05	0.12	-2.01	-3.56	9.12	1.11
321451	6.90	0.20	-13.44	0.01	-0.50	-2.57	9.31	0.77
321490	6.79	0.45	-14.02	0.01	-1.09	-2.99	9.37	1.01
321492	5.00	0.19	7.73	-0.53
331052	4.74	0.09	-13.65	0.01	-1.03	-2.83	8.78	0.51
332431	9.61	0.29	-13.50	0.01	-0.53	-2.84	9.64	0.86
332640	9.60	0.29	-14.35	0.03	-1.30	-3.61	9.62	0.85
332761	3.88	0.03	-14.41	0.02	-1.60	-3.27	8.57	0.45
332786	12.10	0.51	8.57	-0.24
332844	10.54	0.26	-13.98	0.02	-0.57	-2.99	9.64	0.77
332861	10.48	0.54	-14.64	0.04	-1.60	-3.80	9.40	0.74
332879	6.73	0.20	-14.36	0.05	-1.32	-3.37	9.31	0.79
332887	4.65	0.17	-14.21	0.01	-1.40	-3.15	9.19	0.98
332906	7.65	0.08	-14.20	0.04	-0.96	-3.19	9.58	0.89
333224	9.57	0.58	-14.39	0.06	-1.37	-3.46	9.50	0.96
333318	17.89	0.18	-14.02	0.06	-0.58	-3.49	9.95	0.57
333442	13.26	0.32	-14.04	0.02	-0.82	-3.39	9.65	0.61
748648	5.42	0.35	-14.54	0.03	-1.17	-2.95	9.69	1.45
748715	3.03	0.38	-15.13	0.07	-2.25	-3.50	9.16	1.45
748723	17.70	0.70	-13.84	0.03	-0.48	-2.95	9.61	0.68
748724	9.63	0.20	-14.10	0.03	-0.90	-3.27	9.60	0.77
748737	5.83	0.20	-14.85	0.11	-1.87	-3.80	9.54	1.15
748738	2.27	0.26	-14.76	0.04	-2.28	-3.36	8.61	1.07
748744	3.44	0.46	-14.52	0.02	-1.85	-3.15	9.02	1.26
748757	5.14	0.58	-13.80	0.01	-1.32	-2.86	9.32	1.32
748763	5.44	0.16	-14.73	0.03	-1.24	-3.13	9.90	1.55
748765	2.24	0.20	-12.72	0.01	-0.35	-1.45	8.63	1.07
748766	10.21	0.33	-14.40	0.08	-0.93	-3.27	9.89	1.09
748767	3.56	0.08	-15.30	0.14	-2.74	-4.31	8.84	0.81
748769	3.47	0.20	-14.51	0.04	-1.97	-3.45	8.76	0.82
748770	11.99	0.35	-14.31	0.07	-0.88	-3.34	9.71	0.78
748777	13.85	0.41	-14.12	0.02	-0.58	-3.13	9.88	0.87
748778	0.15	0.20	-13.99	0.04	-3.69	-2.46	6.36	1.13
748786	7.91	0.78	-13.87	0.01	-1.11	-2.75	9.15	1.05
748788	2.87	0.05	-13.66	0.01	-0.95	-2.34	8.85	1.00
748790	4.78	0.70	8.82	1.03
748794	4.70	0.20	9.13	0.93
748795	10.04	0.48	-14.18	0.04	-0.79	-3.01	9.64	0.96
748798	6.55	0.20	-15.40	0.34	-2.01	-4.05	9.55	1.06
748805	8.71	0.17	-14.77	0.08	-2.25	-4.54	8.74	-0.02
748815	4.13	0.39	-14.03	0.01	-1.17	-2.68	9.23	1.25
748817	4.82	0.29	-14.18	0.02	-1.33	-3.04	9.17	0.99
748819	6.39	0.20	8.78	0.31

of SFR and gas mass. Generally, the gas in a normal galaxy consists of ionized, atomic, and molecular gas. Since our sample is an HI-selected sample and lacks molecular observations, we just calculate $\text{SFE}_{\text{H I}}$ as follows:

$$\text{SFE}_{\text{H I}} = \frac{\text{SFR}}{M_{\text{H I}}}. \quad (10)$$

The distributions of the SFR, $\text{SFE}_{\text{H I}}$, and Σ_{SFR} , $\Sigma_{\text{H I}}$ are shown in Figure 9. For comparison, we also show the distributions for samples of star-forming and starburst galaxies.

In panels (a) and (b), star-forming galaxies are derived from Young et al. (1996), and starburst galaxies are from Jaskot et al. (2015). In panels (c) and (d), both star-forming galaxies and starburst galaxies are derived from Kennicutt (1998b). Compared with star-forming and starburst galaxies, both the SFR and SFE of LSBGs are lower than those of star-forming galaxies by approximately one order of magnitude, and even lower than those of starburst galaxies. Furthermore, the SFR surface densities Σ_{SFR} of LSBGs are more than one order of magnitudes lower than those of star-forming galaxies.

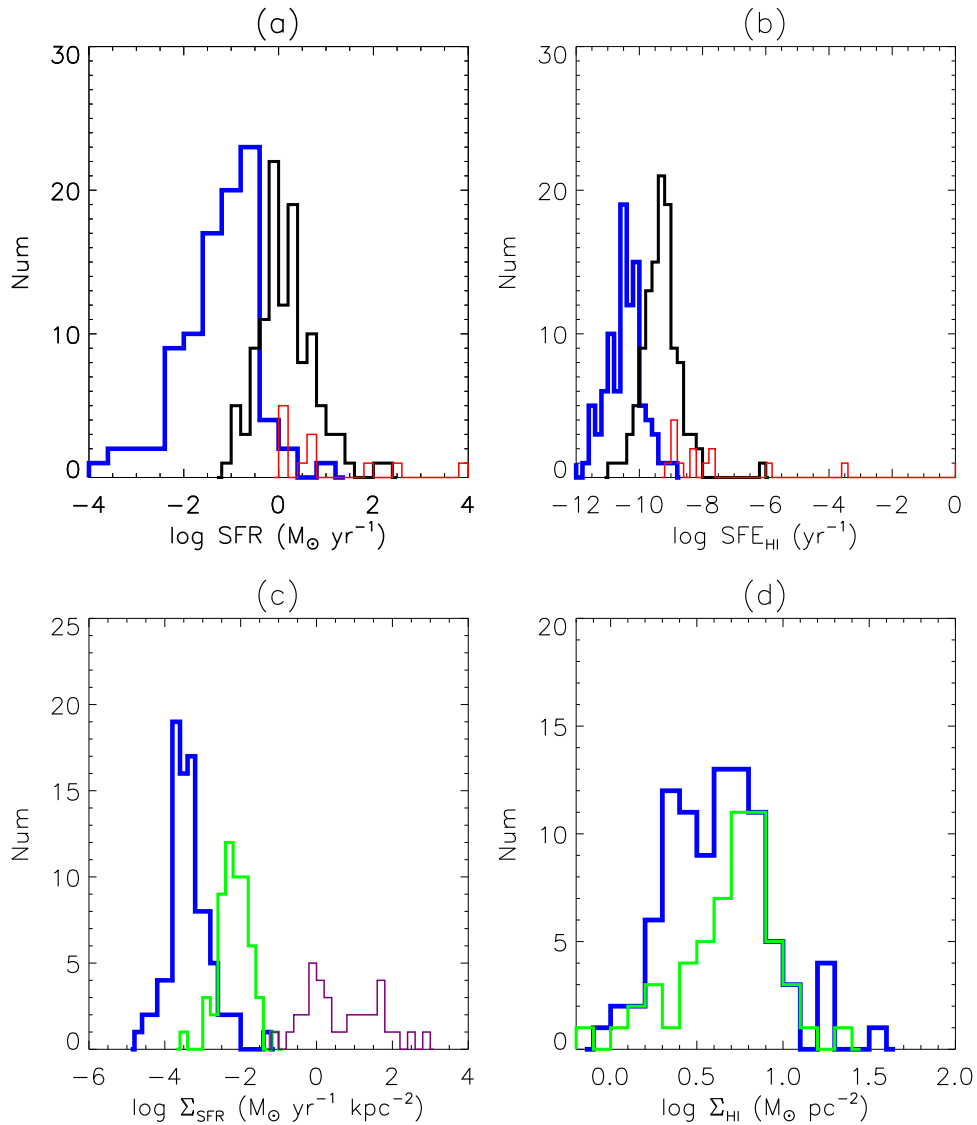


Figure 9. Distributions of (a) star formation rate; (b) star formation efficiency, $SFE = SFR/\text{mass}(\text{H I})$; (c) star formation surface density; (d) gas (H I) surface density. Blue represents the LSBGs in this paper. The black and red colors in (a) and (b) represent star-forming galaxies from Young et al. (1996) and starburst galaxies from Jaskot et al. (2015). Green ((c)) and purple ((d)) represent star-forming galaxies and starburst galaxies from Kennicutt (1998b), respectively.

4.2. Kennicutt–Schmidt Law

Figure 10 shows the relation between SFR surface density and H I surface density (Σ_{HI}). The blue symbols are star-forming (disk) galaxies from Kennicutt (1998b). The red circles are galaxies belonging to the Local supercluster (Gavazzi et al. 2012) and the black points are LSBGs in our sample. The orange stars are LSBGs from Wyder et al. (2009). Following O’Neil et al. (2003), we plot dotted lines with SFEs of 1%, 10%, and 100% in a timescale of star formation of 10^8 yr, corresponding to typical orbital timescales in galaxies. The Kennicutt–Schmidt law is plotted as a black solid line. The coverage of our LSBGs is similar to that of Wyder et al. (2009) LSBGs, but is toward even lower star formation surface density. From Figure 10, LSBGs and star-forming galaxies are in the same region of H I surface density, but LSBGs have much lower SFR surface densities than star-forming galaxies. Galaxies in the Local Supercluster have a more diffuse Σ_{HI} distribution.

Several previous works tried to detect CO emission in LSBGs. However, most of them only gave upper limits on CO

content, and a few LSBGs detected molecular gas. (Matthews & Gao 2001; O’Neil et al. 2003; Matthews et al. 2005; Das et al. 2010). Cao et al. (2017) observed the CO (2-1) of nine LSBGs from Du2015 with JCMT, but none of them detected CO (2-1) emission, so only upper limits M_{H_2} are given. The $M_{\text{H}_2}/M_{\text{HI}}$ ratios are less than 0.02, which indicates a shortage of molecular gas in LSBGs (Cao et al. 2017).

Bigiel et al. (2008) derived a correlation between SFR surface brightness density and H_2 surface density,

$$\Sigma_{\text{SFR}} = 10^{-2.1 \pm 0.2} \Sigma_{\text{H}_2}^{1.0 \pm 0.2}, \quad (11)$$

which helps us to estimate the approximate H_2 surface density from this relation. Even though H_2 gas is not distributed as the H I gas (Leroy et al. 2008; Lisenfeld et al. 2011), Equation (11) can be used as a rough estimation of Σ_{H_2} . To get accurate values, future interferometric H I and CO data are necessary. From Figure 11, gas surface density $\Sigma_{\text{HI}+\text{H}_2}$ (red circles) is very close to Σ_{HI} (black dots), which is consistent with our previous assumption: H I dominates the gas content of our LSBGs.

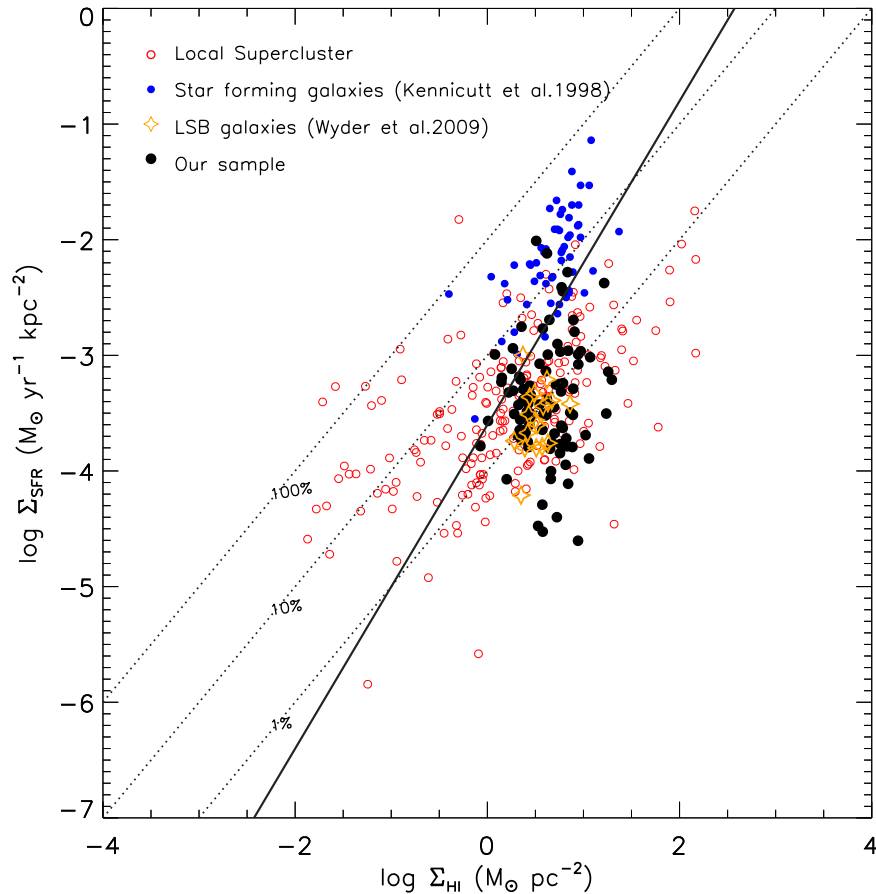


Figure 10. Relation between SFR surface density and H I surface density. The black dots are from this paper, the yellow diamonds are LSBGs from Wyder et al. (2009), and the blue dots are star-forming galaxies from Kennicutt (1998b). The red circles are galaxies in the Local Supercluster in the H α 3 survey from Gavazzi et al. (2012). The black solid line is the Kennicutt–Schmidt Law, and the three dotted lines show the H I SFEs of 100%, 10%, 1% on a timescale of star formation of 10^8 yr.

All LSBGs are located at the cutoff region, deviating from the Kennicutt–Schmidt law (black line), which is derived from the star-forming (blue dots) and starburst galaxies (green dots).

According to the dashed line (SFE), starburst galaxies have SFEs that are higher than 10%, and star-forming galaxies have SFEs a little lower than 10%, but still much higher than 1%. Though a small number of LSBGs are blended with star-forming galaxies, LSBGs have SFEs far below those of star-forming galaxies and of around 1% for most of them. In some extreme cases, SFE can even be lower than 0.1%. There is a special LSBG, AGC 748765, whose SFE is far above 10%. It has an extremely luminous H II region in its disk.

Kennicutt & Evans (2012) pointed out that the gas surface density can crudely be divided into three regions: low density ($\Sigma_{\text{gas}} < 10 M_{\odot} \text{pc}^{-2}$), intermediate density ($10 M_{\odot} \text{pc}^{-2} < \Sigma_{\text{gas}} < 100\text{--}300 M_{\odot} \text{pc}^{-2}$), and high density ($\Sigma_{\text{gas}} > 100\text{--}300 M_{\odot} \text{pc}^{-2}$). Although the SFR surface density of LSBGs can spread more than three orders of magnitudes, their gas surface densities are in a narrow region within one order of magnitude from 1 to $10 M_{\odot} \text{pc}^{-2}$. The SFR surface density of LSBGs does not show any dependence on gas or H I surface density. The brown line is the upper limit for the low-density region in Figure 11. The mean gas surface density for LSBGs in our sample ($\Sigma_{\text{gas}} = 4.1 M_{\odot} \text{pc}^{-2}$) is shown as a pink line in Figure 11. As expected, LSBGs are located in the low-density region. However, many star-forming galaxies are also located in the low-density region, but with higher SFR density. The tight relation between SFR and molecular gas

(Gao & Solomon 2004; Bigiel et al. 2008) demonstrates that the molecular gas could still dominate the gas in star-forming galaxies. From Figure 11, the turnoff point of the K–S Law is around $\Sigma_{\text{gas}} = 4 M_{\odot} \text{pc}^{-2}$, which is almost the lowest gas density among star-forming galaxies, and also a similar value to the mean gas surface density of LSBGs. What causes the SFR surface density to be widely distributed in such low-density regions is worth exploring in future work.

4.3. Star Formation History

To characterize the evolutionary status of the star formation in galaxies, we follow specific (sSFR = SFR/ M_*) and H I depletion time ($t_{\text{dep}}(\text{H I}) = M_{\text{H I}}/\text{SFR}$) to study the star formation history of LSBGs. Stellar mass is derived from g - and r -band magnitudes from Du2015 and follows the equation $\log(M_*/M_{\odot}) = -0.306 + 1.097 * (g - r) + \log L_r/L_{\odot}$ (Bell et al. 2003). H I depletion time and sSFR relation are shown in Figure 12. The red circles are galaxies from the Local Supercluster (Gavazzi et al. 2012) and the black solid circles are our LSBGs. The dashed line representing the sSFR value is -10.1367 , which means a galaxy can gain current stellar mass in current SFR throughout Hubble time. Here, Hubble time is adopted with 13.7 Gyr (Spergel et al. 2007). The dashed line is the boundary between the active phase of galaxies and the quiescent phase.

On average, the current SFRs in the Local Supercluster cannot account for their current masses, though they present

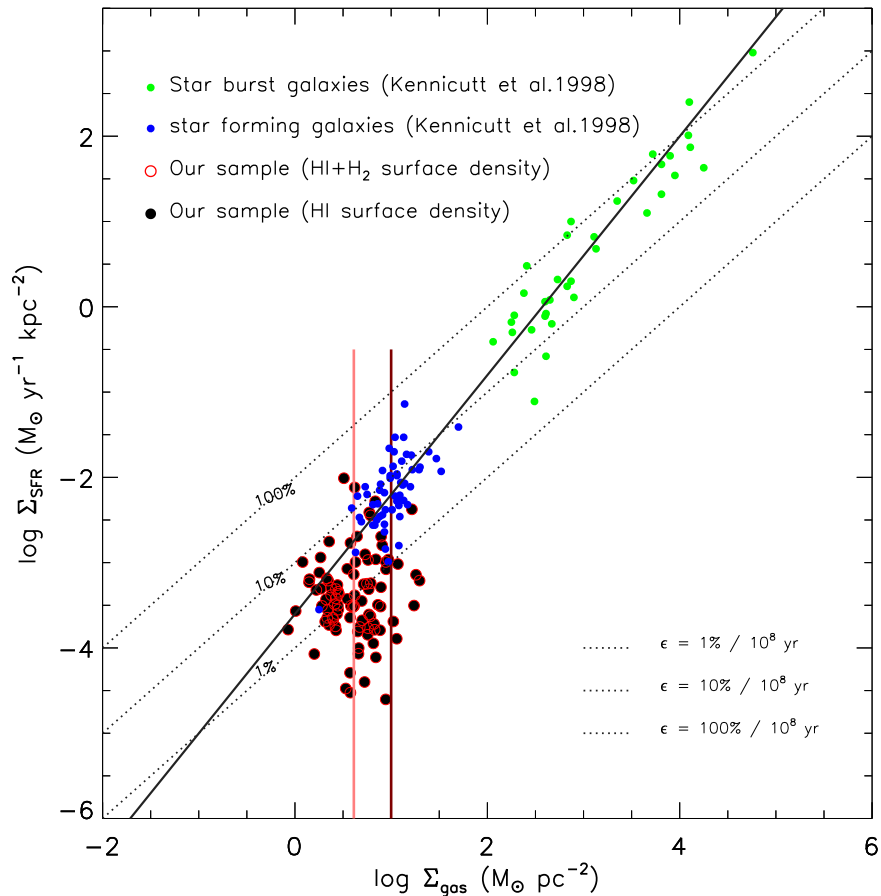


Figure 11. Relation between SFR surface density and H I surface density. Our LSBG sample is the black solid circle (H I gas surface density) and red circles (gas surface density). The blue dots are star-forming galaxies and the green dots are starburst galaxies; both are from Kennicutt (1998b). The black solid line is the Kennicutt–Schmidt Law, and the three dotted lines show the H I SFEs of 100%, 10%, 1% on a timescale of star formation of 10^8 yr. The pink line is the mean value of the LSBG gas surface density and the brown dashed line is the upper boundary of the low gas surface density of $10 M_{\odot} \text{pc}^{-2}$.

higher SFRs than those of LSBGs. Galaxies in the Local Supercluster should experience intensive star formation events once or several times in their star formation histories. Most LSBGs are around the dashed line in Figure 12 and some LSBGs are active phase galaxies. Even with low current SFRs, most LSBGs can still obtain the current stellar mass over the timescale of universe. They do not need a strong interacting or major merging process to occur. A stochastic and sporadic star formation scenario could explain such low and stable star formation histories (de Blok et al. 1995; Lam et al. 2015). The lower number density environment of LSBGs may indicate that they seldom experience galactic interactions or mergers (Du et al. 2015). This is supported by the stellar populations with ages around 2 Gyr in LSBGs (Du et al. 2017). The higher $t_{\text{dep}}(\text{H I})$ of our LSBGs suggest that they will have an abundant supply of H I in the future.

5. Summary

We performed a narrow band H α imaging survey for LSBGs selected from the 40% ALFALFA extragalactic H I survey. A sample of 111 LSBGs in the fall sky has been observed with the Xinglong 2.16 m telescope. The LSBGs in this sample have recession velocities ranging from 1012 to 9889 km s $^{-1}$ and H I masses from $\log_{10} M_{\text{H I}} = 7.73$ to $\log_{10} M_{\text{H I}} = 10.14$. H α fluxes of 92 objects are measured using IRAF ellipse photometry. The derived total H α fluxes and corresponding

SFRs are listed in Table 3. All the LSBGs in our sample have blue features that are similar to those of other LSBG samples. They have lower SFRs, lower SFEs, lower star formation surface densities, lower gas surface densities, and similar H I surface densities compared with normal star-forming galaxies.

Most LSBGs are in low surface density regions and are below the Kennicutt–Schmidt relation. Their SFR surface densities spread about three orders of magnitude and their SFE efficiencies are around 1% or even lower. To characterize the star formation histories of LSBGs, we adopt parameters of $t_{\text{dep}}(\text{H I})$ and sSFR. From the distribution of both parameters, LSBGs tend to be gas-rich and their star formation histories tend to be stable, rarely suffering from intensive interaction or major mergers.

We thank the referee for constructive comments and suggestions. This project is supported by the National Key R&D Program of China (No. 2017YFA0402704), and the National Natural Science Foundation of China (grants No. 11733006, 11403037, 11225316, 11173030, 11303038, 11403061, and U1531245), the China Ministry of Science and Technology under the State Key Development Program for Basic Research (2014CB845705), and the Strategic Priority Research Program, The Emergence of Cosmological Structures of the Chinese Academy of Sciences (grant No. XDB09000000). This project is also supported by the China Ministry of Science and Technology under the State Key

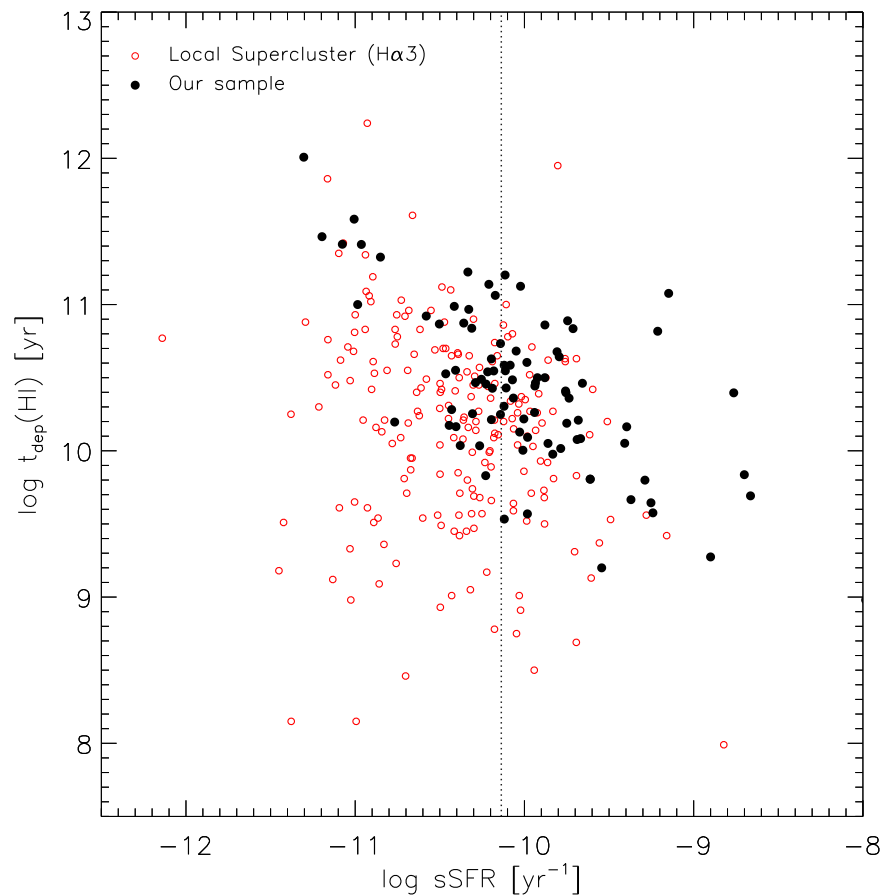


Figure 12. $t_{\text{dep}}(\text{HI})$ vs. sSFR diagram. The black solid circles are our LSBG sample, and the red open circles are galaxies in the Local Supercluster from the H α 3 survey (Gavazzi et al. 2012).

Development Program for Basic Research (grant No. 2014CB845705).

We acknowledge the support of the staff of the Xinglong 2.16 m telescope. This work is partially supported by the Open Project Program of the Key Laboratory of Optical Astronomy, National Astronomical Observatories, Chinese Academy of Sciences. We also thank the ALFALFA team and the SDSS team for the released data. The Arecibo Observatory is part of the National Astronomy and Ionosphere Center, which is operated by Cornell University under a cooperative agreement with the National Science Foundation. The authors acknowledge the work of the entire ALFALFA collaboration team in observing, flagging, and extracting the catalog of galaxies used in this work. The ALFALFA team at Cornell is supported by NSF grant AST-0607007 and AST-1107390 and by grants from the Brinson Foundation. The authors are thankful for the useful SDSS database and the MPA/JHU catalogs. Funding for the SDSS has been provided by the Alfred P. Sloan Foundation, the Participating Institutions, the National Science Foundation, the U.S. Department of Energy, the National Aeronautics and Space Administration, the Japanese Monbukagakusho, the Max Planck Society, and the Higher Education Funding Council for England.

ORCID iDs


Wei Du  <https://orcid.org/0000-0003-4546-8216>

Yi-Nan Zhu  <https://orcid.org/0000-0002-2798-2783>

Man-I Lam  <https://orcid.org/0000-0002-1727-4070>

Zhi-Min Zhou  <https://orcid.org/0000-0002-4135-0977>

Tian-Wen Cao  <https://orcid.org/0000-0002-1335-6212>

Pin-Song Zhao  <https://orcid.org/0000-0002-4328-538X>

Chao-Jian Wu  <https://orcid.org/0000-0003-3514-6619>

References

- Abazajian, K. N., Adelman-McCarthy, J. K., Agüeros, M. A., et al. 2009, *ApJS*, **182**, 543
- Bell, E. F., Barnaby, D., Bower, R. G., et al. 2000, *MNRAS*, **312**, 470
- Bell, E. F., McIntosh, D. H., Katz, N., & Weinberg, M. D. 2003, *ApJS*, **149**, 289
- Bertin, E., & Arnouts, S. 1996, *A&AS*, **117**, 393
- Bigiel, F., Leroy, A., Walter, F., et al. 2008, *AJ*, **136**, 2846
- Bigiel, F., Leroy, A., Walter, F., et al. 2010, *AJ*, **140**, 1194
- Blanton, M. R., Lupton, R. H., Schlegel, D. J., et al. 2005, *ApJ*, **631**, 208
- Boissier, S., Boselli, A., Ferrarese, L., et al. 2016, *A&A*, **593**, A126
- Boissier, S., Gil de Paz, A., Boselli, A., et al. 2008, *ApJ*, **681**, 244
- Boselli, A., Boissier, S., Cortese, L., et al. 2009, *ApJ*, **706**, 1527
- Broeils, A. H., & Rhee, M.-H. 1997, *A&A*, **324**, 877
- Calzetti, D. 2001, *PASP*, **113**, 1449
- Cao, T.-W., Wu, H., Du, W., et al. 2017, arXiv:1708.01362
- Cardelli, J. A., Clayton, G. C., & Mathis, J. S. 1989, *ApJ*, **345**, 245
- Ceccarelli, L., Herrera-Camus, R., Lambas, D. G., Galaz, G., & Padilla, N. D. 2012, *MNRAS*, **426**, L6
- da Cunha, E., Charlot, S., & Elbaz, D. 2008, *MNRAS*, **388**, 1595
- Das, M., Boone, F., & Viallefond, F. 2010, *A&A*, **523**, A63
- de Blok, W. J. G., van der Hulst, J. M., & Bothun, G. D. 1995, *MNRAS*, **274**, 235
- Du, W., Wu, H., Lam, M. I., et al. 2015, *AJ*, **149**, 199
- Du, W., Wu, H., Zhu, Y., Zheng, W., & Filippenko, A. V. 2017, *ApJ*, **837**, 152

- Fossati, M., Gavazzi, G., Savorgnan, G., et al. 2013, *A&A*, **553**, A91
- Freeman, K. C. 1970, *ApJ*, **160**, 811
- Frei, Z., & Gunn, J. E. 1994, *AJ*, **108**, 1476
- Gao, Y., & Solomon, P. M. 2004, *ApJS*, **152**, 63
- Gavazzi, G., Consolandi, G., Viscardi, E., et al. 2015, *A&A*, **576**, A16
- Gavazzi, G., Fumagalli, M., Fossati, M., et al. 2013, *A&A*, **553**, A89
- Gavazzi, G., Fumagalli, M., Galardo, V., et al. 2012, *A&A*, **545**, A16
- Gerritsen, J. P. E., & de Blok, W. J. G. 1999, *A&A*, **342**, 655
- Giovanelli, R., Haynes, M. P., Kent, B. R., et al. 2005, *AJ*, **130**, 2598
- Haynes, M. P., Giovanelli, R., Martin, A. M., et al. 2011, *AJ*, **142**, 170
- He, Y. Q., Xia, X. Y., Hao, C. N., et al. 2013, *ApJ*, **773**, 37
- Huang, S., Haynes, M. P., Giovanelli, R., et al. 2012, *AJ*, **143**, 133
- Huang, S., Haynes, M. P., Giovanelli, R., et al. 2014, *ApJ*, **793**, 40
- Impey, C., & Bothun, G. 1997, *ARA&A*, **35**, 267
- Impey, C., Burkholder, V., & Sprayberry, D. 2001, *AJ*, **122**, 2341
- Jaskot, A. E., Oey, M. S., Salzer, J. J., et al. 2015, *ApJ*, **808**, 66
- Jimmy, Tran, K.-V., Saintonge, A., et al. 2016, *ApJ*, **825**, 34
- Kennicutt, R. C., & Evans, N. J. 2012, *ARA&A*, **50**, 531
- Kennicutt, R. C., Jr. 1998a, *ARA&A*, **36**, 189
- Kennicutt, R. C., Jr. 1998b, *ApJ*, **498**, 541
- Lam, M. I., Wu, H., Yang, M., et al. 2015, *MNRAS*, **446**, 4291
- Leroy, A. K., Lee, C., Schruba, A., et al. 2013, *ApJL*, **769**, L12
- Leroy, A. K., Walter, F., Brinks, E., et al. 2008, *AJ*, **136**, 2782
- Lisenfeld, U., Espada, D., Verdes-Montenegro, L., et al. 2011, *A&A*, **534**, A102
- Lisker, T., Grebel, E. K., Binggeli, B., & Glatt, K. 2007, *ApJ*, **660**, 1186
- Lupton, R. H., Jurić, M., Ivezić, Z., et al. 2005, *BAAS*, **37**, 1384
- Mathews, L. D., & Gao, Y. 2001, *ApJL*, **549**, L191
- Mathews, L. D., Gao, Y., Uson, J. M., & Combes, F. 2005, *AJ*, **129**, 1849
- McGaugh, S. S., Schombert, J. M., & Bothun, G. D. 1995, *AJ*, **109**, 2019
- Noll, S., Burgarella, D., Giovannoli, E., et al. 2009, *A&A*, **507**, 1793
- O'Neil, K., & Bothun, G. 2000, *ApJ*, **529**, 811
- O'Neil, K., Schinnerer, E., & Hofner, P. 2003, *ApJ*, **588**, 230
- Peng, C. Y., Ho, L. C., Impey, C. D., & Rix, H.-W. 2002, *AJ*, **124**, 266
- Schmidt, M. 1959, *ApJ*, **129**, 243
- Schombert, J., Maciel, T., & McGaugh, S. 2011, *AdAst*, **2011**, 143698
- Schombert, J., McGaugh, S., & Maciel, T. 2013, *AJ*, **146**, 41
- Schombert, J. M., Bothun, G. D., Schneider, S. E., & McGaugh, S. S. 1992, *AJ*, **103**, 1107
- Shi, Y., Helou, G., Yan, L., et al. 2011, *ApJ*, **733**, 87
- Silva, L., Granato, G. L., Bressan, A., & Danese, L. 1998, *ApJ*, **509**, 103
- Spector, O., Finkelman, I., & Brosch, N. 2012, *MNRAS*, **419**, 2156
- Spergel, D. N., Bean, R., Doré, O., et al. 2007, *ApJS*, **170**, 377
- Swaters, R. A., & Balcells, M. 2002, *A&A*, **390**, 863
- Van Sistine, A., Salzer, J. J., Sugden, A., et al. 2016, *ApJ*, **824**, 25
- Watson, L. C., Martini, P., Lisenfeld, U., Böker, T., & Schinnerer, E. 2016, *MNRAS*, **455**, 1807
- Wen, X.-Q., Wu, H., Zhu, Y.-N., et al. 2014, *MNRAS*, **438**, 97
- Wu, H., Burstein, D., Deng, Z., et al. 2002, *AJ*, **123**, 1364
- Wu, H., Cao, C., Hao, C.-N., et al. 2005, *ApJL*, **632**, L79
- Wyder, T. K., Martin, D. C., Barlow, T. A., et al. 2009, *ApJ*, **696**, 1834
- Young, J. S., Allen, L., Kenney, J. D. P., Lesser, A., & Rownd, B. 1996, *AJ*, **112**, 1903
- Zheng, Z., Shang, Z., Su, H., et al. 1999, *AJ*, **117**, 2757
- Zhu, Y.-N., Wu, H., Cao, C., & Li, H.-N. 2008, *ApJ*, **686**, 155